ACS APPLIED MATERIALS & INTERFACES

www.acsami.org

Research Article

Unique Contact Point Modification Technique for Boosting the Performance of a Triboelectric Nanogenerator and Its Application in Road Safety Sensing and Detection

Siju Mishra, Muddamalla Rakshita, Haranath Divi,* Supraja Potu, and Rakesh Kumar Rajaboina*

Cite This: *ACS Appl. Mater. Interfaces* 2023, 15, 33095−33108

Read Online

ACCESS | Metrics & More | Article Recommendations | Supporting Information

ABSTRACT: A triboelectric nanogenerator (TENG) is a potential technique that can convert waste kinetic energy to electrical energy by contact separation followed by electrostatic induction. Herein, a unique contact point modification technique has been reviewed carefully via the enlargement of the effective surface area of the tribo layer by using a simple and scalable printing method. In this study, the zinc sulfide (ZnS) nanostructure morphology has been introduced directly on an aluminum electrode (Al) as a tribo positive layer by a modified hydrothermal method and different line patterns directly printed on overhead projector (OHP) transparent sheets by a monochrome laser printer as a tribo negative layer to increase the effective contact area and work-function difference between two tribo layers. This dual parameter results in ∼11 times increment in the open-circuit output voltage (∼420 V) and ∼17 times increment in the short-circuit current density (∼83.33 mA m^{-2}) compared to the normal one. Furthermore, with the proposed surface modification technique, an ultrahigh instantaneous output power density of ∼3.9 W m^{-2} at a load resistance of 2 MΩ was easily achieved. The direct energy conversion efficiency reached up to 66.67% at 2 MΩ load, which is very high compared to other traditional TENGs. Further, the fabricated TENG demonstrated efficacy in novel road safety sensing applications in hilly areas to control vehicle movement. Therefore, the current idea of surface engineering using a laser printer will be helpful for energy-harvesting enthusiasts to develop more efficient nanogenerators for higher energy conversions.

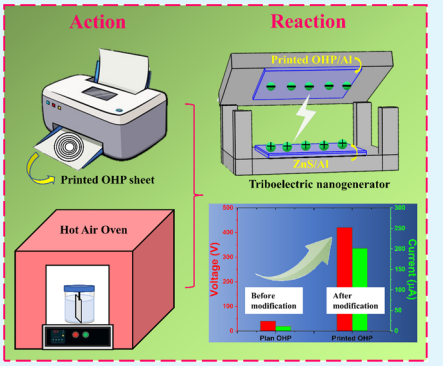

KEYWORDS: *triboelectric nanogenerator, laser printing, surface engineering, contact potential modification, functional material nanostructure*

1. INTRODUCTION

The number of sensors used for the Internet of Things (IoT) is expected to exceed 200 billion by 2025 due to the rapid development of the IoT.[1] As a result, sustainable energy supplies that do not require charging or replacing of charge storage devices are becoming increasingly important. Triboelectricity is one of the oldest areas of scientific study, and it is considered an undesirable effect on the well-being of people and the industry. Many attempts have been made to eliminate and prevent the adverse effects of static electricity. In recent days, triboelectric nanogenerator (TENG) technology has evolved to convert the unwanted contact electrification effect into potential energy-harvesting devices and sensors.[2] Energy sources for TENGs can be found anywhere, on a variety of scales, including wind, tidal movement, touch, breathing, heartbeat, and others.[3−8] The TENG is one of the most promising technologies for delivering a sustainable power source in terms of energy exhaustion and degradation because of its high efficiency, low cost, lightweight, and easy manufacturing process.[9−11] Contact electrification is the main phenomenon behind TENG performance, wherein charge transfer occurs between two dissimilar materials at the contact interface. Based on this phenomenon, TENG has a total of four main working modes: the vertical contact-separation mode (VCSTENG), the lateral sliding mode (LSTENG), the single electrode mode (SETENG), and the free-standing triboelectric layer mode (FSTENG).[12] Because the lifespan of the vertical contact-separation TENG (VCSTENG) mode is typically longer than that of the sliding mode due to less friction damage and the charge generation is also very high compared to other modes, the VCSTENG is mostly used by researchers around the world.[13] Now, the charge generation between two contact surfaces purely depends on the number of contact points between them and the material properties such as work function.[14,15] Researchers have made much effort to increase the TENG output

Received: April 6, 2023
Accepted: May 31, 2023
Published: June 29, 2023

Table 1. Comparison between Different Surface Modification Techniques

materials	modification technique	output	increment in voltage and current (times)	refs
patterned poly(dimethylsiloxane) (PDMS) and patterned Al foil	soft lithography	~230 V, ~15.5 μA cm^{-2}, ~128 mW cm^{-3}		27
sandwich structure of the aluminum film with the PDMS film	photolithography and KOH wet etching	~465 V, ~13.4 μA cm^{-2}, ~53.4 mW cm^{-3}	~2 and ~2.5	28
patterned Au with Kapton	block copolymer (BCP) lithography	~82 μA and ~225 V, ~93.2 W m^{-2}	~16	29
ITO-patterned PDMS	Si wafer molds	~18 V and ~0.7 μA	~4	30
patterned PDMS and aluminum	femtosecond laser direct writing	~42.5 V and ~10.1 μA, ~107.3 μW cm^{-2}	~1.33 and ~1.44	31
Au surface	surface functionalization by chemical functional groups	~240 V, and ~1.75 mA m^{-2}	~4	32
surface modification of PET film	oxygen plasma treatment and forming reactive −OH groups	~330 V and ~270 mA m^{-2}	~4	33
FEP surface	negative ion injection	~1000 V, ~630 μC m^{-2}	~4 and ~5	34
MoS_2 monolayer sheet	electron-trapping material	~52.8 V and ~5.7 μA	~2.4 and ~7.8	35
scratched Al surface and PET	ZnS on scratched Al surface	~262 V and ~56 μA, ~1.325 W/m^2	~4.6 and ~5	15
ZnS and OHP	laser printing on OHP	~420 V, ~83.33 mA m^{-2}, ~3.9 W/m^2	~11 and ~17	current work

performance by enhancing charge generation, including refinement of its structure, surface morphology, surface modifications, introduction of innovative materials, and charge pumping technology.[16−18] Therefore, here, in the current study, an insulated polymeric material with different work functions (OHP, overhead projector sheet) has been introduced as a tribo negative layer between two electrodes, resulting in a higher surface charge density between two tribo layers.[19,20] Electrons strive to fill the lowest possible states when two materials are forced to come together at a near-atomic distance, which is the fundamental driving force behind contact electrification. Thus, significantly overlapping electron wave functions allow for electron transitions.[21] In simple terms, more work-function differences generate more surface charge between two layers. Modifying the particulate layer can significantly and considerably improve the charge-trapping ability of TENG.[22,23] In addition, surface modifications of frictional layers in the micro or nano range also increase the contact points, which leads to an increase in output performance. Therefore, researchers focused on different micro/nano patterns on the tribo-surface to improve the charge generation by scratching, plasma etching, chemical lithography, and laser surface patterning.[24−26] However, these techniques are time-consuming, expensive, very difficult for large-area processing, and have repeatability issue as shown in the comparison in Table 1. In our previous work, we demonstrated the effect of manual scratching on a plane Al surface with emery paper as well as the effect of increased concentration of ZnS nanosheet on TENG performance. However, manual scratching was not the most optimal way to create the roughness.[15] Therefore, in this study, the simplest, fastest, least expensive, and most optimized method has been explored to process the tribo-surface through simple surface modifications to further boost the output performance. Creating uniform surface patterns on an OHP sheet with a simple two-dimensional (2D) laser printer leads to an improvement in surface roughness in a controlled way as shown in the comparison in Table 1.

In turn, the presence of magnetite (Fe_3O_4) and some polymeric materials in the toner powder further affects the overall work function of the OHP sheet. Due to the change in the work function, the charge generation inside the nanogenerator was greatly improved.[36]

In addition, a zinc sulfide (ZnS) nanosheet (NS) film was also introduced as another tribo layer to further enhance the contact points by a modified hydrothermal method. The reasons for adopting the ZnS NS film as another frictional layer are (i) ZnS has piezoelectric and triboelectric capabilities but it has not been as thoroughly studied as ZnO, $BaTiO_3$, CdSe, GaN, and PZT;[37−39] (ii) in terms of TENG design, ultrathin ZnS NSs with a high surface-area-to-volume ratio can also significantly increase the charge-transfer rate between two tribo layers;[40] and (iii) the ZnS nanostructure can be engineered to exhibit specific material properties, such as a high dielectric constant, high electrical conductivity, or tunable surface properties. Thus, overall, these properties can be tailored to optimize the performance of TENG systems, including improving the charge storage capacity, reducing leakage currents, or enhancing the efficiency of energy conversion. In addition, the production of ZnS-based TENG fabrication offers different advantages: (i) no additional electrode deposition step is required for the growth of ZnS NS since they grow directly on the aluminum substrate, (ii) no additional seed layer is required for the growth of ZnS NS compared to seed layer-assisted ZnS nanorod/nanowire growth,[41] and (iii) nanosheets are also mechanically very stable under high pressure.[42] On the other hand, the OHP sheet is a transparent PET material with a precharge on one side to receive the ink particles.[43] Charges on the OHP sheet increase TENG performance and reduce the surface ion injection step. Further, OHP sheets are inexpensive compared to other triboelectric layers such as PTFE, PVDF, silicone, and FEP.

Both of the above modifications boosted the output performance and the charge transfer. These approaches were incredibly practical and inexpensive and most importantly allowed for large surface areas to be modified without size restrictions. This study mainly focused on the effect of selecting a precharged OHP layer and surface-modified OHP sheet by creating different patterns using a 2D laser printer to increase the surface contact points and wok-function difference between two tribo layers. This study opens a new TENG design and operation strategy that represent a significant step

https://doi.org/10.1021/acsami.3c04848
ACS Appl. Mater. Interfaces 2023, 15, 33095−33108

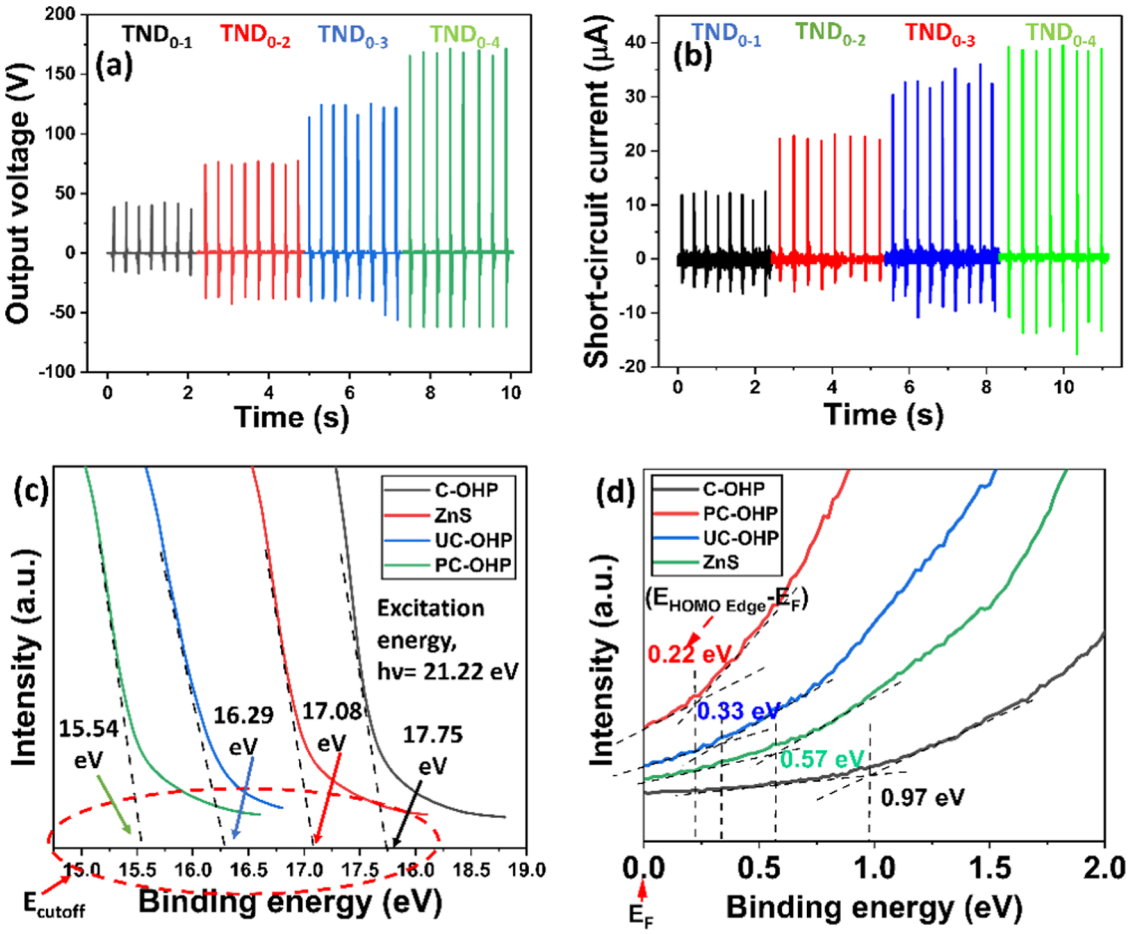

Figure 1. (a) Open-circuit output voltage comparison, (b) short-circuit current comparison, (c, d) UPS spectra of charged OHP sheet, ZnS, uncharged OHP sheet, and printed OHP sheet.

toward the commercialization and application of the technologies.

2. EXPERIMENTAL SECTION

2.1. Materials. The aluminum foil with a thickness of 0.05 mm and a purity of 99% was brought from Special Metals Pvt. Ltd., India, and transparent OHP sheets (~100 μm) were brought from the local market. Anhydrous zinc chloride ($ZnCl_2$), thiourea (NH_2CSNH_2), and ethylenediamine ($C_2H_4(NH_2)$) were brought from FINAR and used without further purifications. Further, sponge, IC 74LS73, inductors, and some different colors of LEDs were purchased from the local market.

2.2. Surface Patterning Using a 2D Laser Printer. The main idea behind this work is to increase the surface contact points by introducing different line patterns on the OHP sheet. The surface pattern of the A4-size OHP sheet was made with a 2D laser printer (Ricoh sp210su) and then cut into an area of 5 × 5 cm^2. Laser printers read the electronic data from the computer and beam that information onto a drum inside the printer, creating a pattern of static electricity (slightly positive). This draws a dry powder (slightly negative) called toner onto the paper, which is then fused using heated rollers. The series of parallel lines with different line widths and with almost constant spacing between the lines were printed on the OHP sheet. The above process was repeated for other patterns such as cross-parallel lines, circular lines, and further different dot patterns as well. All real-time images of the printed OHP sheet with different patterns have been provided in Figure S1 of the Supporting File SI.

2.3. Synthesis of ZnS Nanosheets (NSs). The synthesis of ZnS NSs on planer aluminum is similar to that in previous reports.[15,38] In a typical synthesis procedure, zinc chloride and thiourea in a 1:3 ratio were combined with an aqueous solution of ethylenediamine (1:1), and the whole system was stirred rapidly and agitated for 30 min using a magnetic stirrer. In the well-mixed solution, an Al substrate was placed over the mixed solution in a glass beaker and placed in a hot air oven at 160 °C for 4 h for the direct growth of ZnS NSs. After the growth duration, the whole solution was allowed to cool down to room temperature and the substrate was removed, washed with DI water, and dried under infrared (IR) illuminations. A white coating was formed over the Al substrate.

2.4. Fabrication of TENG. ZnS NS arrays and OHP sheets were used as frictional layers in the TENG, and aluminum substrates were used as conductive electrodes. The lower aluminum substrate was covered with an OHP sheet. In a typical experiment, we used cardboard cut into a 12 × 12 cm^2 rectangular shape for structural support. The aluminum foil (bottom electrode) of the chosen size (5 × 5 cm^2) was then attached to the cardboard with double-sided adhesive tape. The aluminum substrate containing ZnS NSs was then used as the top electrode and connected to the upper cardboard with the ZnS side facing down. Using a couple of sponge spacers, both cardboard sheets were placed one over the other to create a 1 cm gap between two contact layers. Subsequently, the same method was used to fabricate the other TENGs based on surface-patterned OHP sheets (printed OHP sheet) as shown in Supporting Figure S2 in the SI.

2.5. Material Characterizations. An optical microscope was used to measure the thickness of the OHP sheet and the width and interline spacing of line patterns. The surface roughness of the surface-patterned OHP sheets was measured using a stylus profilometer (Handy surf E-35B). The surface work function was measured using ultraviolet (UV) photoelectron spectroscopy (PHI Versa Probe III). The optical images were taken with a digital optical

https://doi.org/10.1021/acsami.3c04848
ACS Appl. Mater. Interfaces 2023, 15, 33095−33108

microscope (LEICA S9i) and an optical microscope (QASMO, QX4RT), each with different magnifications. The shape and composition of surface-patterned OHP sheets were examined using a scanning electron microscope (SEM; VEGA3 TESCAN) and an X-ray diffraction microscope (XRD, X-pert Pro-PW 3050/50). A digital oscilloscope (Tektronix TBS1102) and a low-noise current preamplifier (SR570, Stanford research system) were used to measure the open-circuit output voltage and the short-circuit current. The finite-element simulation of TENG was also performed with the COMSOL Multiphysics 5.6 version. All of the data related to material characterization are available in the Supporting File Figure S3−S5.

3. RESULTS AND DISCUSSION

To simplify our study, this article is divided into three parts; in the first part, we use a commercial transparent OHP sheet with a precharged surface and an uncharged surface to observe the effect of the work-function difference on the output performance of TENG. Second, we introduced line patterns on the OHP sheet surface to increase the contact points. Finally, dot patterns were also introduced to increase the contact points further.

3.1. Plane OHP Sheet-Based TENGs. During the whole experiment, the hand tapping force was ∼6−7 N (Figure S6, in the Supporting File SI) with a tapping frequency of ∼3 Hz. In the first set of experiments, TENGs were tested based on the combination of plane Al and ZnS NSs on the Al with the OHP sheet ink-receptive side and the opposite side, respectively, as shown in Figure S7, in the Supporting File SI. TENGs were fabricated based on both sides of the OHP sheet as a frictional layer to understand the effect of the ink-receptive layer on the TENG performance. Figure 1a,b shows the measured open-circuit voltage (V_o) and short-circuit current (I_s) of different TENG devices: (i) plane aluminum and OHP sheet normal side (TND_{0-1}), (ii) Al with ZnS and OHP normal side (TND_{0-2}), (iii) plane Al and OHP ink-receiving side (TND_{0-3}), and (iv) Al with ZnS and OHP ink-receiving side (TND_{0-4}), with the open-circuit voltages being around 40, 75.2, 121.4, and 168.3 V, and the short-circuit currents being about 11.9, 22.4, 32.9, and 38.8 μA, respectively. From Figure 1, it can be seen that the OHP sheet (ink-receptive side) and ZnS frictional layers played a significant role in enhancing the output performance owing to the extra charge on the OHP ink-receptive surface.[43] The above statement is also experimentally verified in Supporting Video (SV) V1.

3.2. Role of Work Function (WF). To verify the incremental nature of the fabricated TENG's (TND_{0-4}) output voltage and current, UV photoelectron spectroscopy (UPS) was performed to determine the work function of the ZnS NSs on the Al surface and OHP sheet with both sides, respectively. The study shows that the average work function of ZnS NSs was 4.14 eV. Furthermore, we performed the same study for OHP sheet surfaces to measure the work function (WF) of the uncharged surface of the OHP sheet (UC-OHP) and the precharged side of the OHP sheet (C-OHP) as well. As shown in Figure 1c,d, the work function from the UPS secondary electron cutoff data was calculated and is shown in Table 2. The work functions of all of the samples were calculated by using the formula $\phi = h\nu - (E_{cutoff} - E_F)$, where $h\nu$ is the excitation energy 21.22 eV, $(E_{cutoff} - E_F)$ is the binding energy at the secondary electron cutoff, and ϕ is the work function.[44] Thus, by following the mentioned equation, the work functions for the charged OHPs were $\phi_{C\text{-}OHP}$ = 21.22−17.75 = 3.47 eV, ϕ_{ZnS} = 21.22−17.08 = 4.14 eV, $\phi_{UC\text{-}OHP}$ = 21.22−16.29 = 4.93 eV, and $\phi_{PC\text{-}OHP}$ = 21.22−15.54 = 5.68 eV.

Table 2. E_{cutoff} and Work Functions of Different OHP Sheet Surfaces

samples	E_{cutoff} (eV)	Φ (eV)
charged OHP sheet (C-OHP)	17.75	3.47
ZnS	17.08	4.14
uncharged OHP sheet (UC-OHP)	16.29	4.93
printed OHP sheet (PC-OHP)	15.54	5.68

The WF is proportional to the lowest thermodynamic energy required to transfer an electron to infinity from the surface of the solid. Due to this reason there is a difference in WF between two sides of the OHP sheet is mainly due to the existence of some precharge on one side (ink-receptive side), which in turn reduced the surface work function of that side because of the availability of free charges. As depicted in Figure S8a, in the Supporting File SI, the electron clouds of the two materials remain separate without overlapping when two materials (material A and material B) are separated from each other. Because at this point, the electrons are strongly bound in particular orbitals by the potential well, preventing them from easily escaping. When two mentioned materials come close to each other due to the physical interaction between the atoms of two different materials, the electron clouds overlap with each other and eventually form ionic or covalent bonds. The bond length is further compressed when an external compressive force is applied, converting the initial single potential into an asymmetric double-well potential. Tribo-electrification occurs when the powerful electron clouds of electrons overlap, lowering the energy barrier between the two atoms, allowing electrons to pass from one to the other. Thus, the lower WF materials can easily contribute electrons to the other high WF materials when they come atomically close to each other.

In addition, to check the polarity of the charges, we used the band diagram as shown in Figure S8b, in the Supporting File SI, which is for the combination of ZnS NSs and OHP sheets (charged and uncharged). In a charged OHP sheet combination, the electrons go from the OHP sheet surface to the ZnS surface to fill the vacant surface states when they come into contact with each other. For an uncharged OHP sheet combination, an opposite charge polarity appeared, confirming that one side of the OHP sheet (ink-receptive) surface has some precharges. To increase the contact points between two tribo layers, the OHP sheet charged surface was printed with different line patterns by using a 2D monochrome laser printer. The measured average WF for OHP printed on charge side (PC-OHP) was around 5.68 eV. Furthermore, the above indication of the polarity of different surfaces was also experimentally verified by using a digital storage oscilloscope (DSO) as shown in Figure 2d and in Supporting Video V2 in the SI. The peak current for both surfaces of the OHP sheet was exactly opposite to each other as shown in the inset in Figure S8c, in the Supporting File SI. In addition, the printed OHP takes electrons from the ZnS surface since its work function is larger than that of ZnS as shown in Figure S8d, in the Supporting File SI. Therefore, from this study, the ZnS and a printed OHP sheet pair were chosen for our further studies to generate maximum charge since the difference between work functions is maximum ($\Delta\Phi \approx$ ∼1.54 eV).

https://doi.org/10.1021/acsami.3c04848
ACS Appl. Mater. Interfaces 2023, 15, 33095−33108

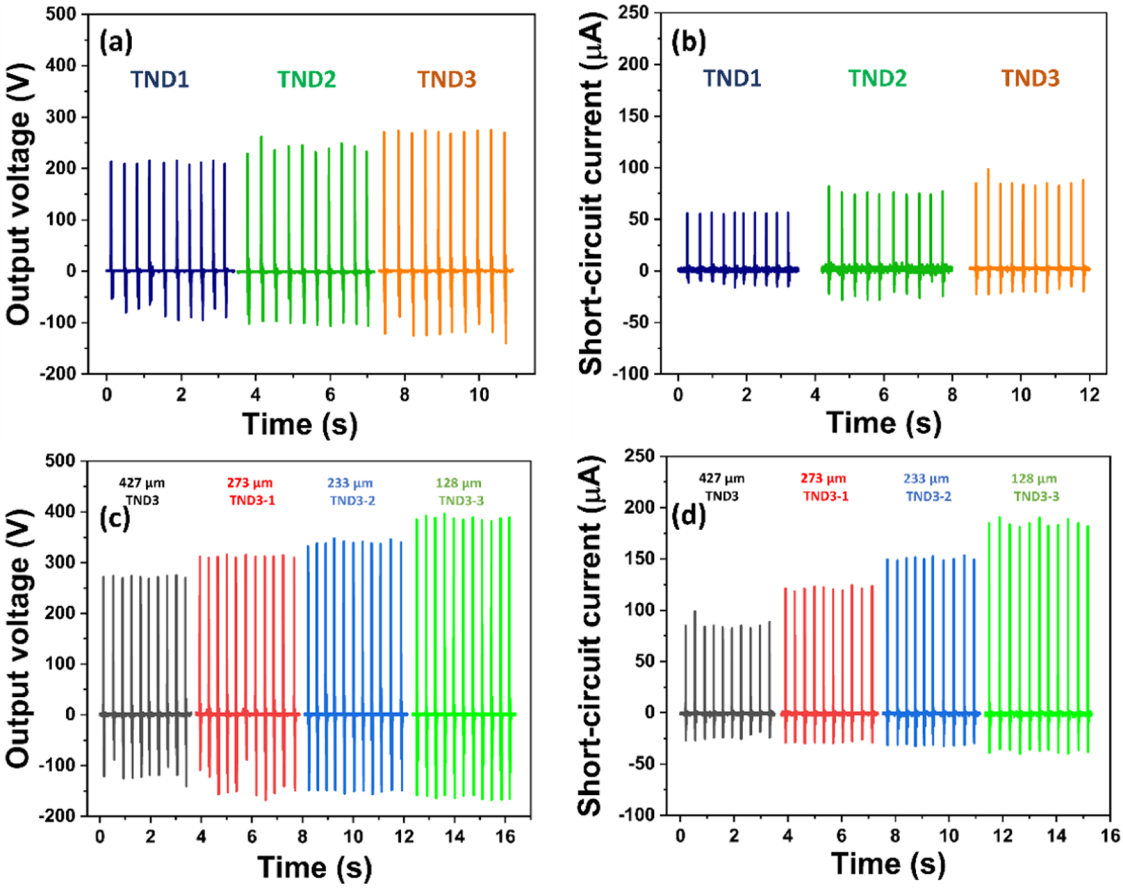

Figure 2. (a) Open-circuit output voltages for different line patterns (straight, circular, and cross-parallel), (b) short-circuit currents for different line patterns (straight, circular, and cross-parallel), (c) open-circuit voltage with reduced line thickness of cross-parallel line pattern, and (d) short-circuit current with reduced line thickness of cross-parallel line pattern.

3.3. Line-Patterned OHP Sheet-Based TENG. In the second series of studies, three TENG devices have been fabricated based on three different types of line patterns, which have been printed directly on the surface of the OHP sheet with a 2D laser printer to create the roughness on the surface and named them TND1, TND2, and TND3. The details of each device are tabulated in Table S1 in the SI. The effect of creating surface roughness on plane OHP is shown in Supporting Video V2, V3. Further, as shown in Figure 2a,b, the V_O and I_S of TND1, TND2, and TND3 increased significantly as the line concentration increased from straight parallel lines to cross-parallel lines. An increased concentration of lines directly affects the surface roughness, which leads to the formation of additional contact points between two tribo surfaces. The voltage and current for TND1 were almost ∼1.27 and ∼1.46 times those of TND_{0-4} because of the increased work-function difference with ZnS as mentioned in Table 2 and increased contact points as well.

The output performances of TND3 were almost ∼1.28 and ∼1.53 times those of TND1 because of increased line concentration per unit area. To further see the effect of line concentration on the output performance of our device, TND3 was further modified with a decreased line width and named as TND3-1, TND3-2, and TND3-3. Since the distance between lines is kept almost constant for all of the line patterns, the number of lines per unit area increased when the width of lines decreased, which in turn increased the contact points. As shown in Figure 2c,d, the output voltage and current of TND3 also increase drastically with decreased line width. The output V_o and I_s of TND3-3 increase by around 1.43 and 2.15 times, respectively, than TND3 and by ∼1.8 and ∼3.3 times, respectively, than TND1 just because additional lines per unit area are generated. Thus, the above study gives a clear idea of how increased contact points affect the output performance of a TENG.

3.4. Dot-Patterned OHP Sheet-Based TENG. The surface contact points have been further modified by implementing different dot patterns printed on the OHP sheet. Thus, here in the third set of study, TENG devices based on different types of dot patterns like straight dots, cross dots, and circular dots have been designed and named TND4, TND5, and TND6, respectively. The details of the mentioned fabricated devices are shown in Table S2 in the SI. As shown in Figure 3a,b, the V_o and I_s for all types of dot patterns increase exactly similar to the study based on the line pattern mentioned above. The V_o and I_s for dot-patterned TENGs were even greater than the previous line-pattern-based respective devices.

The voltage and current of TND6 device were almost ∼1.45 and ∼1.8 times greater than TND1 device. In addition, TND6 was again modified with a decreased dimension of dots. As shown in Figure 3c,d, the V_o and I_s again increased with a decreased width of dots. Again, the output response was larger than its own line-pattern structure. The maximum V_o and I_s for TND6-3 were ∼420 V and ∼201.4 μA, respectively, which were about 2 and 3.6 times higher than those of TND1,

https://doi.org/10.1021/acsami.3c04848
ACS Appl. Mater. Interfaces 2023, 15, 33095−33108

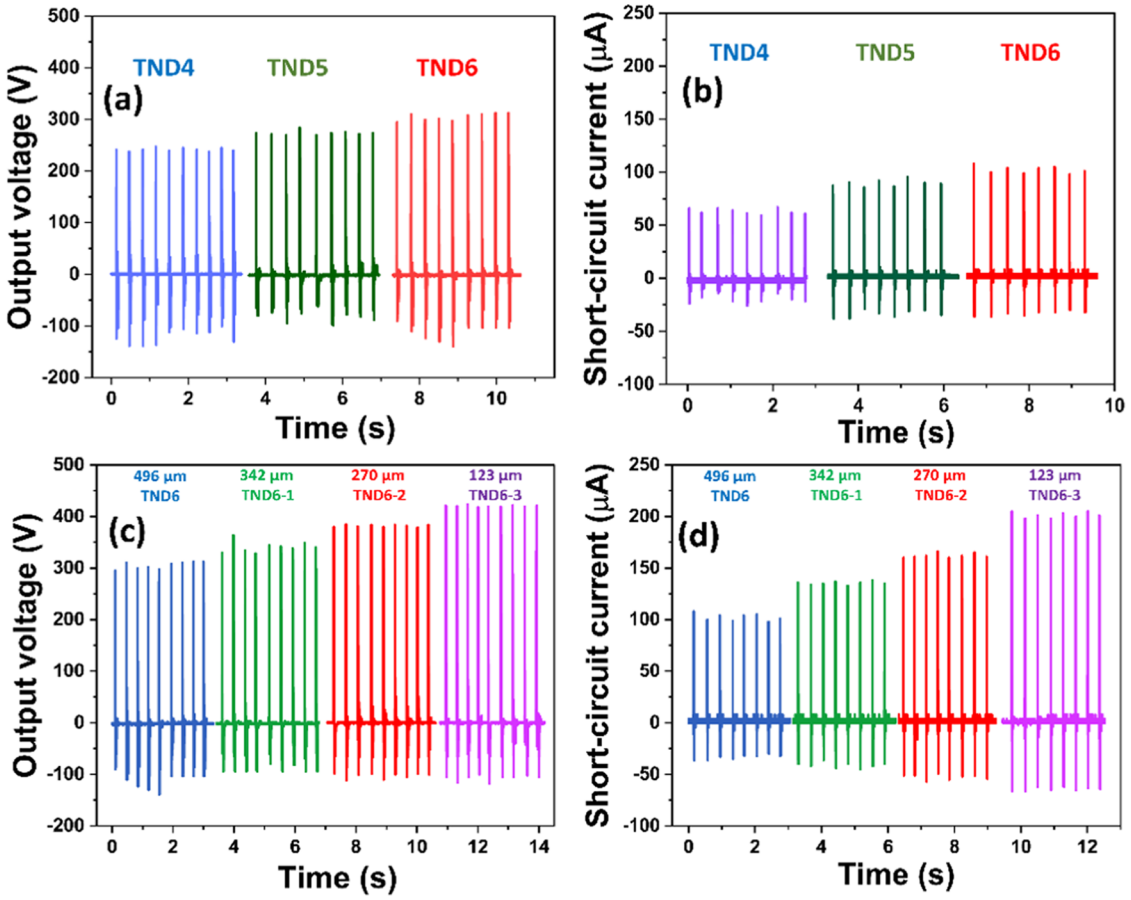

Figure 3. (a) Open-circuit voltages for different dot patterns (straight, circular, and cross-parallel), (b) short-circuit currents for different dot patterns (straight, circular, and cross-parallel), (c) open-circuit voltage with reduced dots size of cross dots patterns, and (d) short-circuit current with reduced dot size of cross dots pattern.

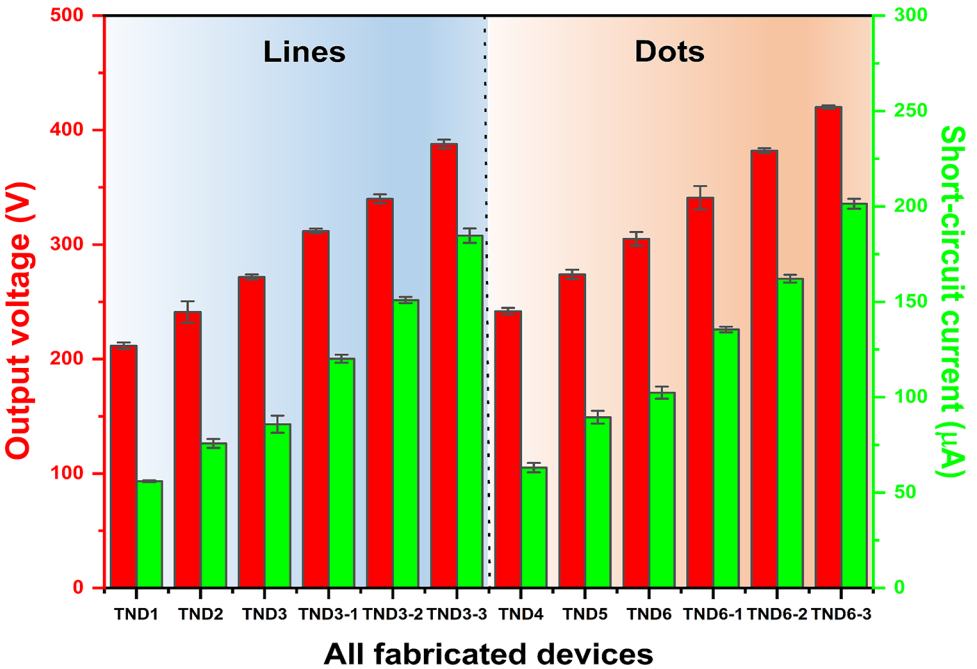

Figure 4. Output performance of all fabricated TENG devices with the line and dot pattern printed on the OHP sheets with ZnS as an opposite triboelectric layer.

respectively. All the output performance values of the fabricated devices are shown in Figure 4 as a bar diagram for

https://doi.org/10.1021/acsami.3c04848
ACS Appl. Mater. Interfaces 2023, 15, 33095−33108

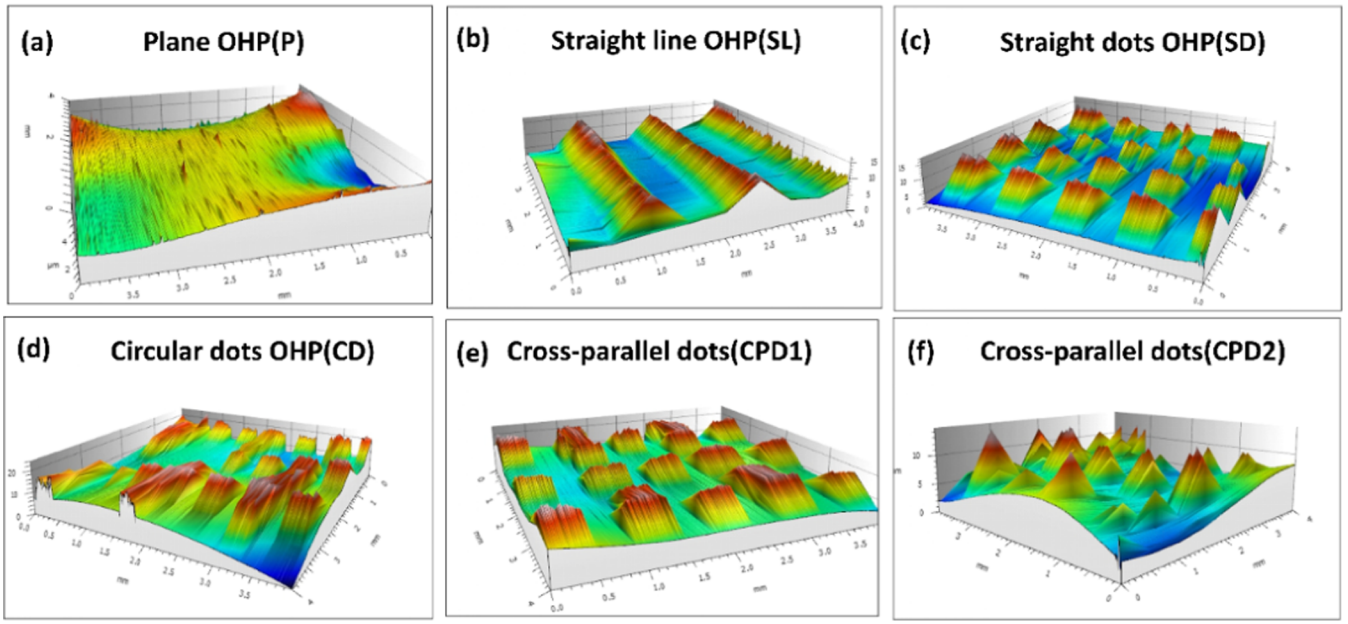

Figure 5. Surface roughness profile of an OHP sheet with (a) no pattern, (b) straight line, (c) straight dot pattern, (d) circular dot pattern, (e) cross-parallel dot pattern (with the highest dimension), and (f) cross-parallel dot pattern with the lowest dimension.

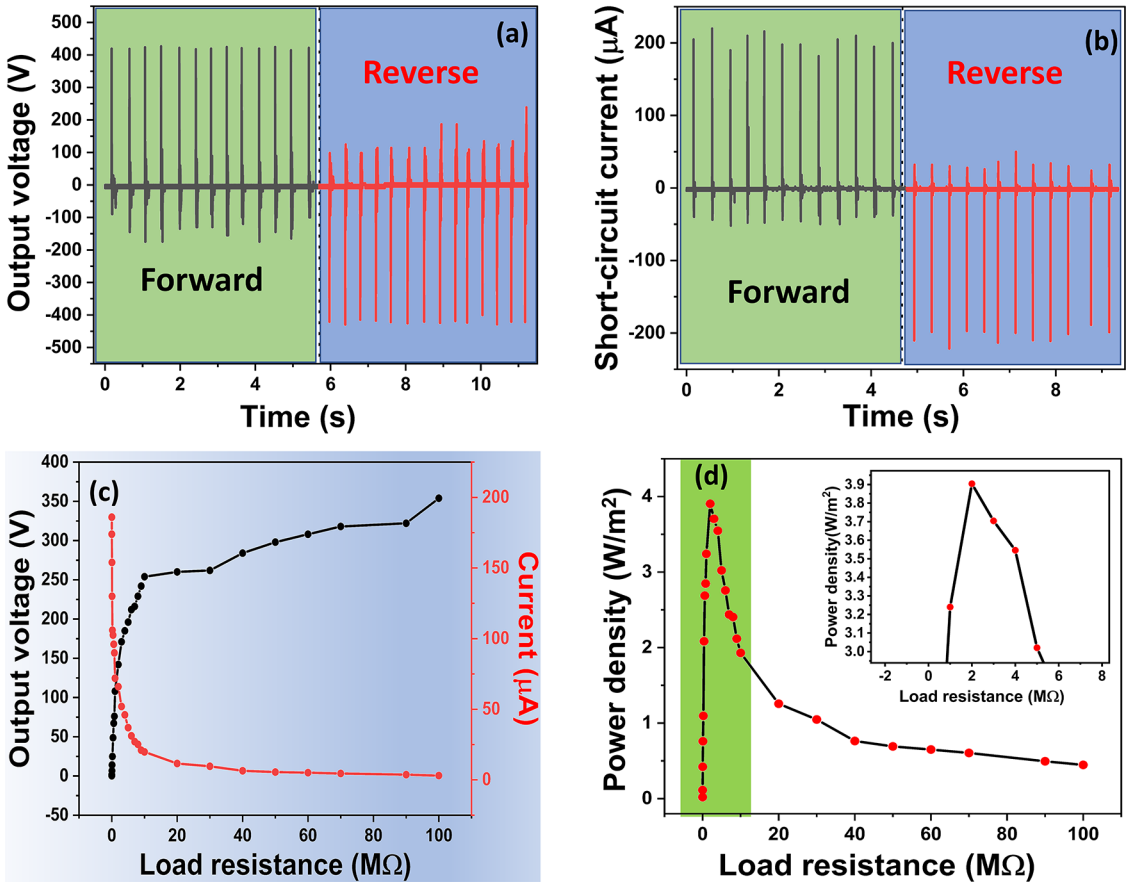

Figure 6. (a) Forward−reverse open-circuit voltage of TND6-3. (b) Forward−reverse short-circuit current of TND6-3. (c) Voltage and current with variable load resistance. (d) Power density with variable load resistance.

comparison, which confirms the fact that the same dot pattern clearly outperforms its own line pattern due to an increase in contact points per unit area between two tribo layers.

In addition, all output response data depending on the lesser width/size for all of the mentioned patterns can be found in Figure S9 in the SI, and a comparison table is also provided in Table S3 in the SI. After all of these above surface treatment-

https://doi.org/10.1021/acsami.3c04848
ACS Appl. Mater. Interfaces 2023, 15, 33095−33108

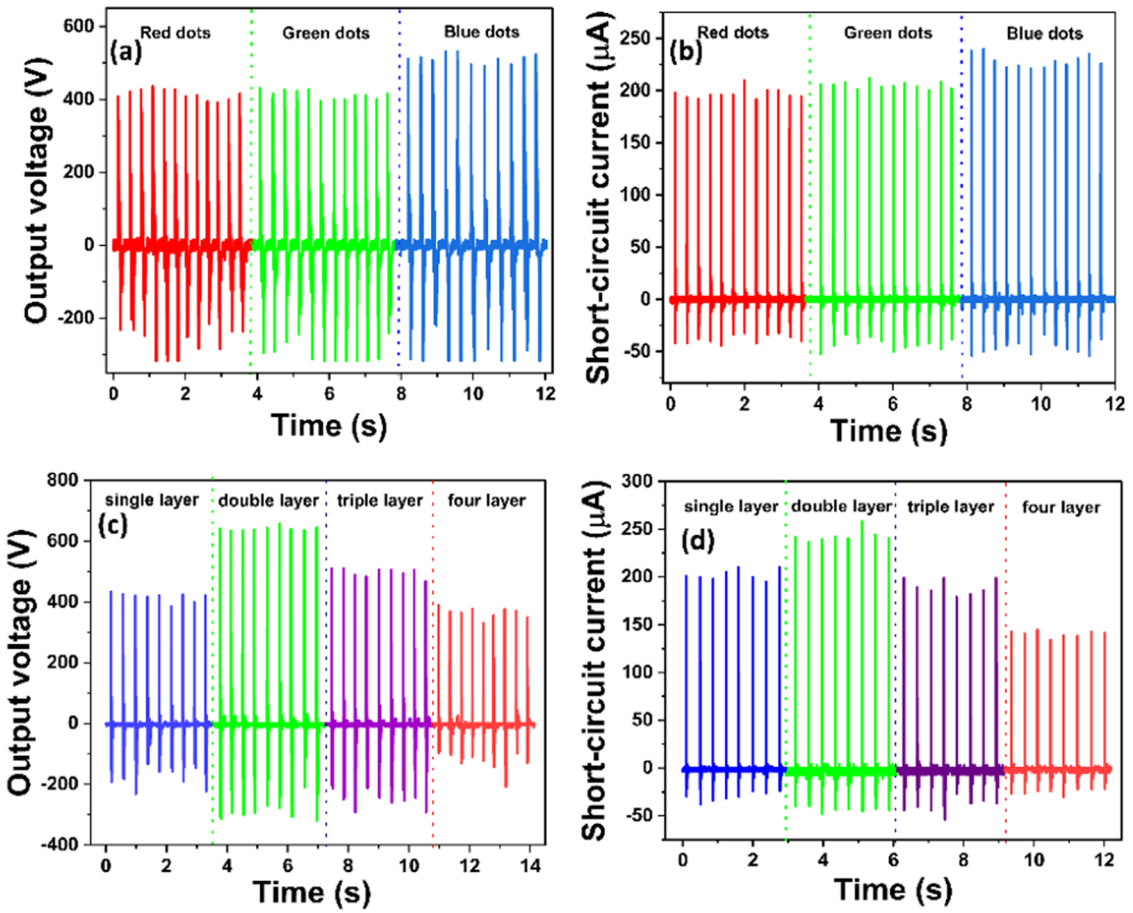

Figure 7. (a) Open-circuit output voltage for RGB dyes with cross-parallel dots (TND6-3), (b) short-circuit current for RGB dyes with cross-parallel dots (TND6-3), (c) open-circuit output voltage with dielectric-layer thickness, and (d) short-circuit current with dielectric-layer thickness.

related studies, TND6-3 was chosen for further nanogenerator electrical characteristic studies in the later section.

In addition, a digital microscopic study was performed to study all of the line and dot patterns as shown in Figure S10 in the SI. The highest line concentration was found for the cross-line pattern in Figure S10a,c in the SI, and it was kept increasing for a decreased width of lines as shown in Figure S10d−f in the SI. The distance between the line was kept almost constant throughout the experiment at ∼1.2 mm. Figure S10g−i in the SI show the different dot patterns and also their respective concentrations. As shown in Figure S10j−l in the SI, the concentration of dots again increased for a lesser dimension. A high-magnification optical microscope of the same patterns was further used to measure the width of all line patterns and dot patterns as shown in Figure S11 in the SI. From this, it can be concluded that the increased number of lines/dots created more contact points between two tribo layers, which in turn justified the increased behavior of voltage and current for all of the samples. This statement is further supported by surface roughness data measured by using a stylus profilometer.

3.5. Surface Roughness. To confirm the actual scientific reason for the increase in output performance, the surface roughness was measured for a few selected samples to see the difference in roughness between two samples using a stylus profilometer. As shown in Figure 5a, the three-dimensional (3D) surface roughness distribution for plane OHP gives an R_a ∼ 24.9 nm. Further, as shown in Figure 5b−c, for a linear dot pattern, the surface roughness significantly suppresses the linear line-pattern OHP sheet, causing an enhancement in output performance as shown in the bar diagram of Figure 4. Furthermore, among all of the dot pattern-based OHP sheets, the cross-parallel dots have the highest roughness value of ∼2 μm as shown in Figure 5e, which further increased to 2.5 μm with a more decreased width of dots (Figure 5f). All of the roughness-related details and their comparison bar graph are available in Figure S12 in the SI. Thus, these roughness values closely supported our previous assumption about the roughness-dependent output performance. We can conclude that the increment in the output performance for different patterns was mainly due to the increase in surface roughness.

3.6. Nanogenerator Characteristics. Since TND6-3 was selected as the best device for testing other TENG general characteristics and also for various applications, TND6-3 was again tested for both forward and reverse connections to verify that the signal is generated by the device itself and not from any noise signal as noise will not change its sign by reversing the connections as shown in Figure 6a,b. To further measure the instantaneous output power density of our fabricated TENG, we first performed voltage response with variable load resistance connected parallel to the device. As shown in Figure 6c, the output voltage increased with increased load resistance up to 100 MΩ because when the load resistance is high, the circuit behaves like an open circuit and all of the charge accumulated across this load resistance result in more potential difference. Figure 6c shows that the output current with

https://doi.org/10.1021/acsami.3c04848
ACS Appl. Mater. Interfaces 2023, 15, 33095−33108

variable load resistance connected to the device (series) was reduced with increased load resistance due to ohmic losses.[45] Because through high load resistance charge could not easily pass, it resulted in a very low current. After calculating the instantaneous power density by using the equation $P = VI/A$ (active area), the maximum output power density was about 3.904 W/m^2 at 2 MΩ of load resistance as shown in Figure 6d. This power density was used to light up RGB LEDs directly. In addition, the stability of the fabricated TENG was tested for over ∼10.5k continuous cycles as shown in Figure S13 in the SI, and the output performance did not degrade after the cyclic test, which confirms the great repeatability of the device. The surface morphology of the used tribo layers (ZnS and printed OHP) before and after stability was also recorded using SEM and an optical microscope as shown in Figure S14 in the SI. Some minor changes in the surface morphology after ∼10.5k cycles did not affect the nanogenerator output voltage as shown in Figure S13 in the SI. Further, the direct conversion efficiency of our fabricated TENG was further calculated by following the procedure described in the literature as shown in Figure S15 in the SI.[46] The efficiency was ∼66.67% at 2 MΩ load resistance, which is the highest efficiency reported so far with the ZnS-based TENG reported to date. Thus, with this unexplored, inexpensive (0.15 $/cm^2, Table S4 file SI), very fast, and most optimized surface modification strategy, one can further boost the output performance of TENG devices.

3.7. Effect of Color Ink on TENG Performance. The TND6-3 was further tested for color-based RGB dot patterns printed on the OHP sheet with a color laser printer (Figure S16 in SI). The effect of red and green dyes on nanogenerator performance was almost similar for voltage and current. However, for blue dyes that were present on these blue dot patterns, additional output was observed compared to black, red, and green. The average open-circuit voltage and short-circuit current for blue dots were around ∼512 V and ∼228 μA, respectively, for a single TENG device (Figure 7a,b). To check the possible reason for this, the dielectric constant for these dots printed with RGB color was measured, which clearly showed that the blue-color material had a higher dielectric constant than the materials with other colors at a fixed frequency (Figure S17 in the SI). According to previous publications,[21,47] the dielectric constant of triboelectric materials plays a significant role in increasing the maximum charge density (σ'), which is defined as follows

$$\sigma' = \frac{\sigma_0 \cdot x(t)}{x(t) + d_{OHP}/\varepsilon_{OHP}}$$

where σ_0 is the equilibrium triboelectric charge density, $x(t)$ is the gap distance (10 mm in this case), and d_{OHP} and ε_{OHP} are the thickness and dielectric constant of the OHP sheet, respectively. Thus, improving the dielectric constant of tribo layers can in turn improve the charge-trapping capacity and promote displacement current generation within triboelectric materials. As a result, increasing the dielectric constant improves both the maximum charge density and the TENG output performance. In order to see the effect of dielectric-layer thickness on the output response of TND6-3, the OHP sheet with a single cross-dot pattern was further modified with an increased number of additional OHP sheets with the same dot patterns. As shown in Figure 7c,d, the open-circuit output voltage and the short-circuit current both first increased with an increase in the number of OHP sheets and then decreased drastically with a further increase in numbers. These results show that the thickness of the OHP sheet has a significant impact on the output voltages and current. This is due to the dual influence of charge transport characteristics and interfacial deformation in the OHP sheet of varying thicknesses. As a result, the output voltage and current tend to rise. However, thickening the OHP sheet increases its rigidity while reducing the interfacial deformation between the two contact materials, resulting in a decrease in the effective contact area. As a result, instead of increasing continuously, the output voltage and current decrease from a certain thickness value. In other words, if the thickness is moderate, the OHP sheet may fully utilize the contact force and expand the interfacial deformation, whereas a thick OHP sheet can constrain its deformation and reduce the effective contact area. As a result, the output voltages and current increased for up to ∼200 μm but then decreased. The other possible reason may be that electric fields from charged TENG surfaces propagate longer distances at higher layer thicknesses to reach the respective electrode−dielectric interfaces, where the induction of output charges takes place, which in turn leads to a decrease in the electric field strength due to their distance-dependent nature. This, in turn, reduces the open-circuit voltage and short-circuit current. Therefore, lower dielectric-layer thicknesses are advantageous for TENGs in terms of obtaining a higher output power.[47−50]

In this study, we further simulate the TENG output performance in the COMSOL simulation to compare the voltage profile of the plane OHP sheet-based TENG with the surface-modified OHP sheet-based TENG. Mathematical modeling of a typical TENG was performed consisting of two electrodes with two dielectric materials: one was ZnS and another one was PET (OHP).[51] Integrating the positive half-cycle of the short-circuit current, the charge quantity transferred for each pulse was calculated as shown in Figure S18 in the SI and further used as a total surface charge density; since the separation distance is much greater than the thickness of the materials, the total charge transferred is equal to the total triboelectric charge. The TENG exhibits capacitive behavior, with the output voltage fluctuating proportionally to the plate spacing. TENG's output voltage is inversely proportional to the capacitance while being directly proportional to the distance between plates.[51,52] Figure S19a−c in the SI depicts the structure of a typical TENG with two dielectric (triboelectric) layers and two metal electrodes, where the distance "D" represents the distance between the two triboelectric layers, its potential difference, and its output voltage with distance. Figure S19d−f in the SI depicts the structure of a TENG with the surface-patterned dielectric layer, its potential difference, and its output voltage with increasing distance in COMSOL. After surface patterning, the output voltage increased tremendously as the surface charge density increased, as shown in Figure S19f in the SI. Compared to simulation results, the fabricated TENG output was very low even after surface patterning because of the insufficient contact area in practical instances and additional losses that are not accounted for, such as air breakdown, electron emission, and combining with induced charges, the simulated potential would be substantially larger than the experimental one.[53−56]

3.8. Applications. The fabricated highly efficient printed TENG (TND6-3) was demonstrated for different electronic applications, for example, a unique road safety sensor system is designed by using TENG. One lab-stage prototype road safety model of the whole experiment has been prepared and shown

https://doi.org/10.1021/acsami.3c04848
ACS Appl. Mater. Interfaces 2023, 15, 33095−33108

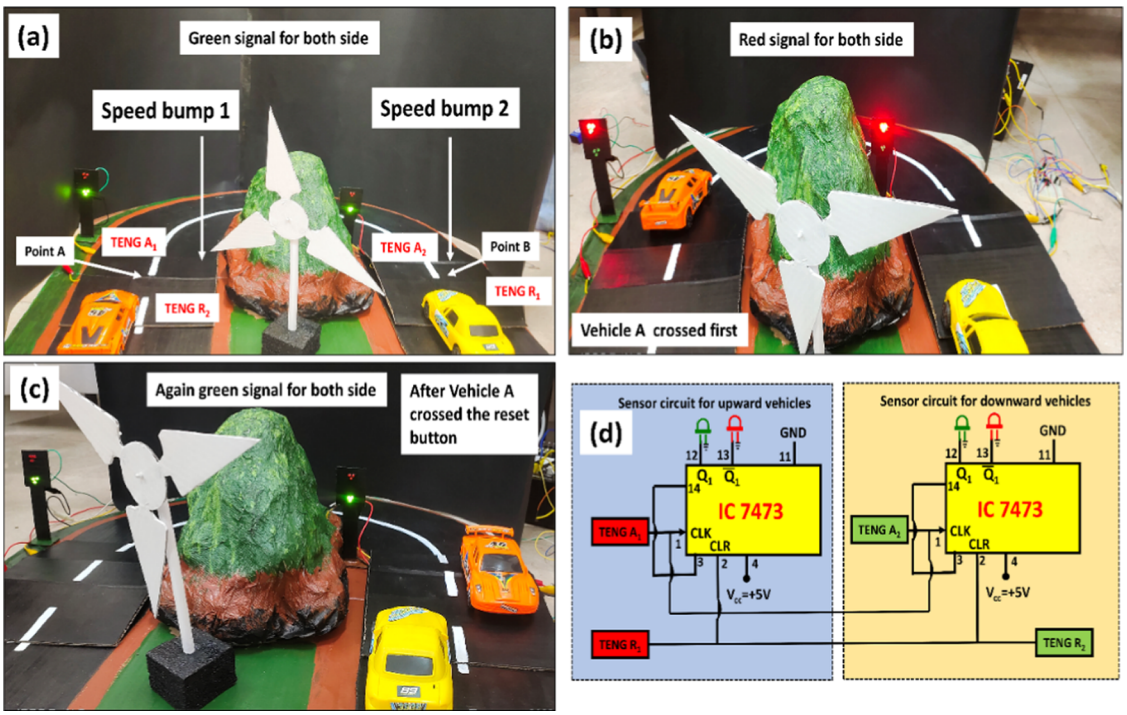

Figure 8. TENG acts as a novel road safety sensor, (a) green signal for upcoming vehicles, (b) red signal when any one vehicle passed (vehicle A), (c) again green signal when vehicle A passed through the reset point, and (d) circuit diagram of the full sensor.

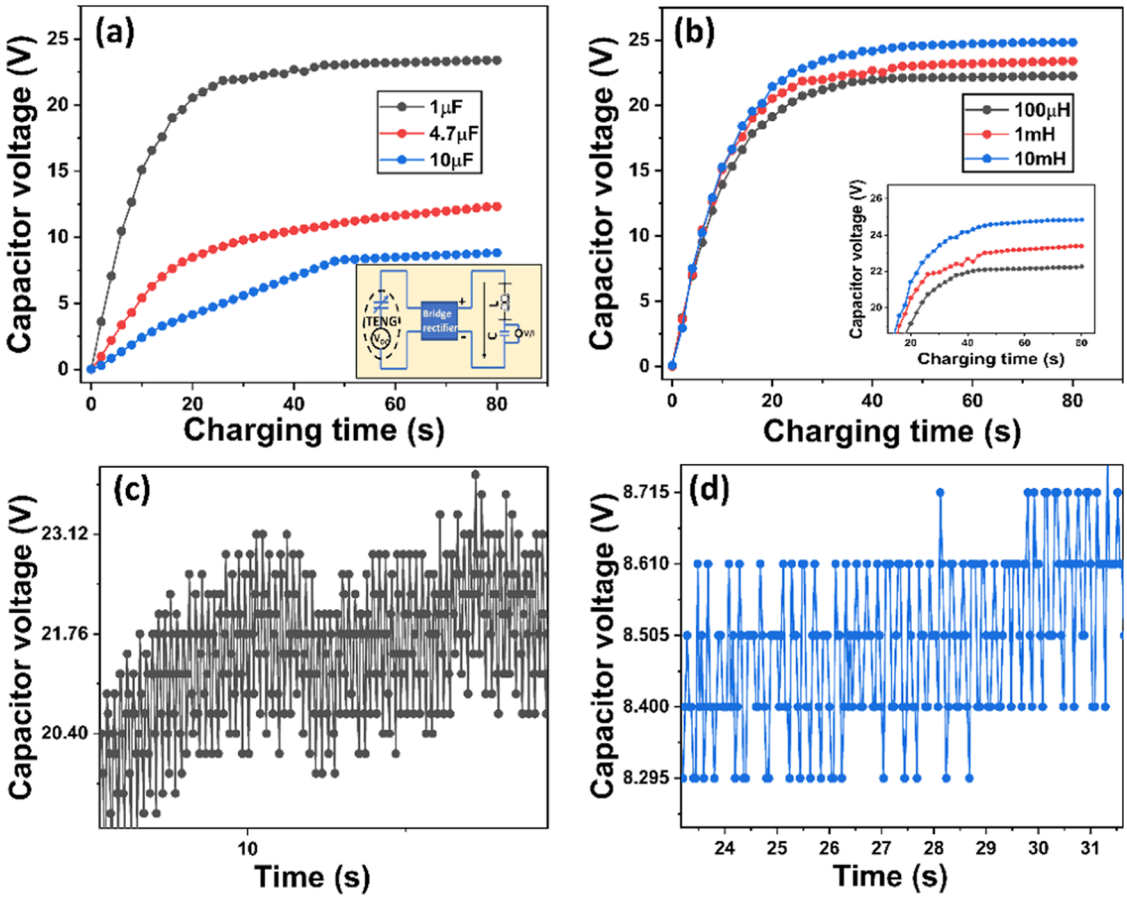

Figure 9. Efficient power management circuit using passive circuit elements, (a) output voltage from the power management circuit with variable capacitance, (b) output voltage from the power management circuit with variable inductance, (c) ripple voltage for the lowest capacitance combination, and (d) ripple voltage for the highest capacitance combination.

https://doi.org/10.1021/acsami.3c04848
ACS Appl. Mater. Interfaces 2023, 15, 33095−33108

in Figure 8 and in the Supporting Video, V4. In hilly areas, driving around a sharp turn is quite risky due to many sharp bends and one-way streets. There are no appropriate signaling systems installed to control the movement of upward- and downward-going vehicles. Thus, in this experiment, we took four 2 × 2 cm^2 TENG for clock pulse generation and installed them under speed breakers, which sent a signal when any vehicle moved on them. A T-type flip-flop circuit was used to operate the signal, which changed its state after every clock pulse. Therefore, initially, both side signals were green for all of the incoming vehicles from both sides (upward and downward) as shown in Figure 8a. When the first vehicle (vehicle A) crossed point "A" as shown in Figure 8b, the TENG generated a clock pulse that changed the state of the T-type flip flop and the green signal turned into red for the rest of the vehicles going up or down. At the end of the curve, when vehicle A crossed the reset TENG installed at point B, the signal again changed from red to green for vehicles on both sides as shown in Figure 8c. Further, when vehicle B crossed point "B", it again changed the state of the circuit, which in turn changed the signal from green to red installed at point "A" and point "B". By repetition of this process, one can control the movement of vehicles in a hairpin bend in any type of hilly area, which will reduce the chances of accidents in the future. The circuit diagram of the whole experiment is shown in Figure 8d. Further, in hilly areas and open places (like highways), wind energy is abundant; one can convert wind energy to mechanical energy and mechanical energy to electrical energy as described in the literature to make the sensor system fully self-powered.[57−59]

To overcome this scenario of pulsed output voltage, we reconstructed one power management circuit based on passive electronic components using a combination of inductor and capacitor including a bridge rectifier because active electronic components increase the power consumption and the complexity in the circuit (inset of Figure 9a).[60] As shown in Figure 9a, our pulsed TENG (TND6-3) was tested to charge different capacitors for up to 80 s by using one 100 μH commercial inductor. The stored voltage in the 1 μF capacitor was the highest among the others because of its lower capacitance value. Further, the constructed power management circuit was also tested to charge one 1 μF capacitor for three different values of inductance as shown in Figure 9b. The magnified image has been provided in the inset of Figure 9b. The stored voltage gradually increased with increasing L value and reached the maximum for the 10 mH inductor. The stray capacitance and resistance in the circuit will consume more energy from the TENG as the equivalent impedance of "L" decreases.[60] After all of these optimizations, a 10 mH inductor and a 10 μF capacitor were chosen because the ripple voltage for the lower capacitor (V_{ripple} = ±2.75 V) was very high as shown in Figure 9c,d. According to Figure S20a in the SI, by using the abovementioned combination one digital watch was turned on after a charging session of ∼12 s and left on for the remaining time. On the other hand, for a digital calculator to switch on continuously, it took ∼18 s of charging time (Figure S20b in the SI) as shown in Supporting Video, V5. Thus, by using this combination, one can generate an almost constant voltage from the vertical contact-separation TENG, which can be more useful than pulsed TENG.

Further, the fabricated TND6-3 was used to drive RGB LEDs connected in series directly without using any power management circuits. As shown in Figure S20c in the SI, 130 RGB LED arrays in the shape of our institute name "NIT" were successfully driven by the TENG (Supporting Video, V6). Further, to verify the output short-circuit current, we connected 675 red LEDs in series, which also lit up (Supporting Video, V7). These experiments prove the capability of the as-fabricated TENG in potential practical applications.

4. CONCLUSIONS

In conclusion, surface potential-modified TENG followed by a novel surface modification technique has been investigated thoroughly for various applications. For the first time, a fully optimized and controlled surface modification technique with great repeatability outcomes has been explored. The maximum voltage from a 5 × 5 cm^2 device was ∼420 V, and the short-circuit current was ∼200 μA. The direct peak power density and the direct energy conversion efficiency were ∼3.9 W m^{-2} and 66.67%, respectively, without using any power management circuits, which was one of the highest values compared to other conventional TENGs. Further, the theoretical values were also simulated by COMSOL Multiphysics software to observe the effect of high contact points. This high power was later used to light up different RGB LEDs connected in series and a huge number of red LEDs as well. In addition, a new application using TENG was also explored, like an intelligent road safety sensing application, for the first time and an efficient passive power management circuit was also constructed to generate constant voltage/current.

■ ASSOCIATED CONTENT

Supporting Information

The Supporting Information is available free of charge at https://pubs.acs.org/doi/10.1021/acsami.3c04848.

Real-time image of various patterns before and after printing, **S-1** (Figure S1); TENG fabrication, **S-2** (Figure S2); morphology characterization details, **S-3** (Figure S3); XRD characterizations, **S-3** (Figure S4); morphology characterization of toner powder, **S-3** (Figure S5); calculation of tapping force, **S-4** (Figure S6); different TENG device structures, **S-5** (Figure S7); charge-transfer polarity and electron cloud model, **S-6** (Figure S8); details of TENG devices for the second set, **S-7** (Table S1); details of TENG devices for the third set, **S-7** (Table S2); comparison of the output with variable width, **S-8** (Figure S9); average output performance for all of the devices, **S-8** (Table S3); low-magnification optical microscopy images, **S-9** (Figure S10); high-magnification optical microscopy images, **S-9** (Figure S11); average roughness of all of the samples, **S-10** (Figure S12); stability test, **S-11** (Figure S13); morphology of tribo layers after the stability test, **S-11** (Figure S14); efficiency calculation, **S-12** (Figure S15); price calculation, **S-13** (Table S4); optical microscope image of different colored dyes, **S-14** (Figure S16); dielectric constant measurement, **S-14** (Figure S17); transferred charge calculation, **S-15** (Figure S18); COMSOL simulation results, **S-16** (Figure S19); and practical applications, **S-17** (Figure S20) (PDF)

Precharge test(OHP) (MP4)

Open-circuit voltage of different OHP surfaces (MP4)

Short-circuit current of different OHP surfaces (MP4)

Road safety device (MP4)

https://doi.org/10.1021/acsami.3c04848
ACS Appl. Mater. Interfaces 2023, 15, 33095−33108

Digital watch_Calculator switch on continuously (MP4)
NIT logo illuminating (MP4)
675 LEDs illuminating (MP4)

AUTHOR INFORMATION

Corresponding Authors

Haranath Divi − *Energy Materials and Devices Laboratory, Department of Physics, National Institute of Technology, Warangal, Warangal 506 004, India;* orcid.org/0000-0002-7936-6165; Email: haranath@nitw.ac.in

Rakesh Kumar Rajaboina − *Energy Materials and Devices Laboratory, Department of Physics, National Institute of Technology, Warangal, Warangal 506 004, India;* orcid.org/0000-0003-4023-9051; Email: rakeshr@nitw.ac.in

Authors

Siju Mishra − *Energy Materials and Devices Laboratory, Department of Physics, National Institute of Technology, Warangal, Warangal 506 004, India;* orcid.org/0000-0003-3774-4196

Muddamalla Rakshita − *Energy Materials and Devices Laboratory, Department of Physics, National Institute of Technology, Warangal, Warangal 506 004, India;* orcid.org/0000-0002-1904-7760

Supraja Potu − *Energy Materials and Devices Laboratory, Department of Physics, National Institute of Technology, Warangal, Warangal 506 004, India;* orcid.org/0000-0001-5612-4035

Complete contact information is available at: https://pubs.acs.org/10.1021/acsami.3c04848

Notes

The authors declare no competing financial interest.
The authors declare that they have no known competing financial interests or personal relationships that could have appeared to influence the work reported in this paper.

ACKNOWLEDGMENTS

The authors R.M. and H.D. are grateful to the Council of Scientific & Industrial Research (CSIR) and the Department of Science and Technology (DST), Government of India, for providing financial support under various projects viz CSIR-SRF #09/0922(11518)/2021-EMR-I and #CRG/2021/007142, respectively. The authors thank CRIF NITW for SEM and XRD studies and Prof. Arockia Kumar for helping in taking optical images. The COMSOL work reported here was supported in part by I-STEM (Indian Science, Technology, and Engineering facilities Map) program funded by the Office of the Principal Scientific Adviser to the Govt. of India.

REFERENCES

(1) Umair, M.; Cheema, M. A.; Cheema, O.; Li, H.; Lu, H. Impact of COVID-19 on IoT Adoption in Healthcare, Smart Homes, Smart Buildings, Smart Cities, Transportation and Industrial IoT. *Sensors* **2021**, *21*, 3838.

(2) Wang, Z. L. Triboelectric Nanogenerators as New Energy Technology and Self-Powered Sensors - Principles, Problems and Perspectives. *Faraday Discuss.* **2014**, *176*, 447−458.

(3) Zhu, G.; Bai, P.; Chen, J.; Lin Wang, Z. Power-Generating Shoe Insole Based on Triboelectric Nanogenerators for Self-Powered Consumer Electronics. *Nano Energy* **2013**, *2*, 688−692.

(4) Shi, B.; Zheng, Q.; Jiang, W.; Yan, L.; Wang, X.; Liu, H.; Yao, Y.; Li, Z.; Wang, Z. L. A Packaged Self-Powered System with Universal Connectors Based on Hybridized Nanogenerators. *Adv. Mater.* **2016**, *28*, 846−852.

(5) Zheng, Q.; Shi, B.; Fan, F.; Wang, X.; Yan, L.; Yuan, W.; Wang, S.; Liu, H.; Li, Z.; Wang, Z. L. In Vivo Powering of Pacemaker by Breathing-Driven Implanted Triboelectric Nanogenerator. *Adv. Mater.* **2014**, *26*, 5851−5856.

(6) Li, Z.; Zhu, G.; Yang, R.; Wang, A. C.; Wang, Z. L. Muscle-Driven in Vivo Nanogenerator. *Adv. Mater.* **2010**, *22*, 2534−2537.

(7) Nguyen, V.; Yang, R. Effect of Humidity and Pressure on the Triboelectric Nanogenerator. *Nano Energy* **2013**, *2*, 604−608.

(8) Vivekananthan, V.; Chandrasekhar, A.; Rao Alluri, N.; Purusothaman, Y.; Khandelwal, G.; Kim, S.-J. Triboelectric Nanogenerators: Design, Fabrication, Energy Harvesting, and Portable-Wearable Applications. In *Nanogenerators*; IntechOpen, 2020.

(9) Saravanakumar, B.; Mohan, R.; Thiyagarajan, K.; Kim, S. J. Fabrication of a ZnO Nanogenerator for Eco-Friendly Biomechanical Energy Harvesting. *RSC Adv.* **2013**, *3*, 16646−16656.

(10) Xie, Y.; Wang, S.; Niu, S.; Lin, L.; Jing, Q.; Yang, J.; Wu, Z.; Wang, Z. L. Grating-Structured Freestanding Triboelectric-Layer Nanogenerator for Harvesting Mechanical Energy at 85% Total Conversion Efficiency. *Adv. Mater.* **2014**, *26*, 6599−6607.

(11) Sukumaran, C.; Viswanathan, P.; Munirathinam, P.; Chandrasekhar, A. A Flexible and Wearable Joint Motion Sensor Using Triboelectric Nanogenerators for Hand Gesture Monitoring. *Int. J. Nanotechnol.* **2021**, *18*, No. 697.

(12) Wang, Z. L. Triboelectric Nanogenerators as New Energy Technology for Self-Powered Chemical Sensors. *ACS Nano* **2013**, 9533−9557.

(13) Bao Han, C.; Du, W.; Zhang, C.; Tang, W.; Zhang, L.; Lin Wang, Z. Harvesting Energy from Automobile Brake in Contact and Non-Contact Mode by Conjunction of Triboelectrication and Electrostatic-Induction Processes. *Nano Energy* **2014**, *6*, 59−65.

(14) Xu, C.; Zhang, B.; Wang, A. C.; Cai, W.; Zi, Y.; Feng, P.; Wang, Z. L. Effects of Metal Work Function and Contact Potential Difference on Electron Thermionic Emission in Contact Electrification. *Adv. Funct. Mater.* **2019**, *29*, No. 1903142.

(15) Mishra, S.; Supraja, P.; Haranath, D.; Kumar, R. R.; Pola, S. Effect of Surface and Contact Points Modification on the Output Performance of Triboelectric Nanogenerator. *Nano Energy* **2022**, *104*, No. 107964.

(16) Wang, X.; Chen, X.; Iwamoto, M. Recent Progress in the Development of Portable High Voltage Source Based on Triboelectric Nanogenerator. *Smart Mater. Med.* **2020**, *1*, 66−76.

(17) Lai, M.; Du, B.; Guo, H.; Xi, Y.; Yang, H.; Hu, C.; Wang, J.; Wang, Z. L. Enhancing the Output Charge Density of TENG via Building Longitudinal Paths of Electrostatic Charges in the Contacting Layers. *ACS Appl. Mater. Interfaces* **2018**, *10*, 2158−2165.

(18) Basith, S. A.; Chandrasekhar, A. COVID-19 Clinical Waste Reuse: A Triboelectric Touch Sensor for IoT-Cloud Supported Smart Hand Sanitizer Dispenser. *Nano Energy* **2023**, *108*, No. 108183.

(19) Bharti, D. K.; Veeralingam, S.; Badhulika, S. An Ultra High Performance, Lead-Free Bi 2 WO 6:P(VDF-TrFE)-Based Triboelectric Nanogenerator for Self-Powered Sensors and Smart Electronic Applications. *Mater. Horiz.* **2022**, *9*, 663−674.

(20) Potu, S.; M, N.; Rajaboina, R. K.; Gollapelli, B.; Vallamkondu, J.; Mishra, S.; Divi, H.; Babu, A.; K, U. K.; Kodali, P. High-Performance and Low-Cost Overhead Projector Sheet-Based Triboelectric Nanogenerator for Self-Powered Cholesteric Liquid Crystal, Electroluminescence, and Portable Electronic Devices. *ACS Appl. Energy Mater.* **2022**, *5*, 13702−13713.

(21) Zou, H.; Guo, L.; Xue, H.; Zhang, Y.; Shen, X.; Liu, X.; Wang, P.; He, X.; Dai, G.; Jiang, P.; Zheng, H.; Zhang, B.; Xu, C.; Wang, Z. L. Quantifying and Understanding the Triboelectric Series of Inorganic Non-Metallic Materials. *Nat. Commun.* **2020**, *11*, No. 2093.

(22) He, X.; Guo, H.; Yue, X.; Gao, J.; Xi, Y.; Hu, C. Improving Energy Conversion Efficiency for Triboelectric Nanogenerator with

Capacitor Structure by Maximizing Surface Charge Density. *Nanoscale* **2015**, *7*, 1896−1903.
(23) Chen, J.; Guo, H.; He, X.; Liu, G.; Xi, Y.; Shi, H.; Hu, C. Enhancing Performance of Triboelectric Nanogenerator by Filling High Dielectric Nanoparticles into Sponge PDMS Film. *ACS Appl. Mater. Interfaces* **2016**, *8*, 736−744.
(24) Jeong, C. K.; Baek, K. M.; Niu, S.; Nam, T. W.; Hur, Y. H.; Park, D. Y.; Hwang, G. T.; Byun, M.; Wang, Z. L.; Jung, Y. S.; Lee, K. J. Topographically-Designed Triboelectric Nanogenerator via Block Copolymer Self-Assembly. *Nano Lett.* **2014**, *14*, 7031−7038.
(25) Fan, F. R.; Lin, L.; Zhu, G.; Wu, W.; Zhang, R.; Wang, Z. L. Transparent Triboelectric Nanogenerators and Self-Powered Pressure Sensors Based on Micropatterned Plastic Films. *Nano Lett.* **2012**, *12*, 3109−3114.
(26) Muthu, M.; Pandey, R.; Wang, X.; Chandrasekhar, A.; Palani, I. A.; Singh, V. Nano Energy Enhancement of Triboelectric Nanogenerator Output Performance by Laser 3D-Surface Pattern Method for Energy Harvesting Application. *Nano Energy* **2020**, *78*, No. 105205.
(27) Wang, S.; Lin, L.; Wang, Z. L. Nanoscale Triboelectric-Effect-Enabled Energy Conversion for Sustainably Powering Portable Electronics. *Nano Lett.* **2012**, *12*, 6339−6346.
(28) Zhang, X.-S.; Han, M. -D.; Wang, R.-X.; Zhu, F.-Y.; Li, Z.-H.; Wang, W.; Zhang, H.-X. Frequency-Multiplication High-Output Triboelectric Nanogenerator for Sustainably Powering Biomedical Microsystems. *Nano Lett.* **2013**, *13*, 1168−1172.
(29) Kim, D.; Jeon, S. B.; Kim, J. Y.; Seol, M. L.; Kim, S. O.; Choi, Y. K. High-Performance Nanopattern Triboelectric Generator by Block Copolymer Lithography. *Nano Energy* **2015**, *12*, 331−338.
(30) Fan, F.; Lin, L.; Zhu, G.; Wu, W.; Zhang, R.; Wang, Z. L. Transparent Triboelectric Nanogenerators and Self-Powered Pressure Sensors Based on Micropatterned Plastic Films. *Nano Lett.* **2012**, *12*, 3109−3114.
(31) Kim, D.; Tcho, I. W.; Jin, I. K.; Park, S. J.; Jeon, S. B.; Kim, W. G.; Cho, H. S.; Lee, H. S.; Jeoung, S. C.; Choi, Y. K. Direct-Laser-Patterned Friction Layer for the Output Enhancement of a Triboelectric Nanogenerator. *Nano Energy* **2017**, *35*, 379−386.
(32) Wang, S.; Zi, Y.; Zhou, Y. S.; Li, S.; Fan, F.; Lin, L.; Wang, Z. L. Molecular Surface Functionalization to Enhance the Power Output of Triboelectric Nanogenerators. *J. Mater. Chem. A* **2016**, *4*, 3728−3734.
(33) Shin, S. H.; Kwon, Y. H.; Kim, Y. H.; Jung, J. Y.; Lee, M. H.; Nah, J. Triboelectric Charging Sequence Induced by Surface Functionalization as a Method to Fabricate High Performance Triboelectric Generators. *ACS Nano* **2015**, *9*, 4621−4627.
(34) Wang, S.; Xie, Y.; Niu, S.; Lin, L.; Liu, C.; Zhou, Y. S.; Wang, Z. L. Maximum Surface Charge Density for Triboelectric Nanogenerators Achieved by Ionized-Air Injection: Methodology and Theoretical Understanding. *Adv. Mater.* **2014**, *26*, 6720−6728.
(35) Wen, R.; Guo, J.; Yu, A.; Zhang, K.; Kou, J.; Zhu, Y.; Zhang, Y.; Li, B. W.; Zhai, J. Remarkably Enhanced Triboelectric Nanogenerator Based on Flexible and Transparent Monolayer Titania Nanocomposite. *Nano Energy* **2018**, *50*, 140−147.
(36) Kumar, U.; Gaikwad, V.; Sahajwalla, V. Transformation of Waste Toner to Iron Using E-Waste Plastics as a Carbon Resource. *J. Cleaner Prod.* **2018**, *192*, 244−251.
(37) Mishra, S.; Supraja, P.; Sankar, P. R.; Kumar, R. R.; Prakash, K.; Haranath, D. Controlled Synthesis of Luminescent ZnS Nanosheets with High Piezoelectric Performance for Designing Mechanical Energy Harvesting Device. *Mater. Chem. Phys.* **2022**, *277*, No. 125264.
(38) Mishra, S.; Potu, S.; Sankar, R.; Kumar, R.; Kodali, P.; Divi, H. A Novel ZnS Nanosheets-Based Triboelectric Nanogenerator and Its Applications in Sensing, Self-Powered Electronics, and Digital Systems. *Mater. Today Commun.* **2022**, *31*, No. 103292.
(39) Veeralingam, S.; Badhulika, S. Ti@MoS2 Incorporated Polypropylene/Nylon Fabric-Based Porous, Breathable Triboelectric Nanogenerator as Respiration Sensor and Ammonia Gas Sensor Applications. *Sens. Actuators, B* **2023**, *380*, No. 133346.
(40) Lin, C.; Zhu, X.; Feng, J.; Wu, C.; Hu, S.; Peng, J.; Guo, Y.; Peng, L.; Zhao, J.; Huang, J.; Yang, J.; Xie, Y. Hydrogen-Incorporated TiS2 Ultrathin Nanosheets with Ultrahigh Conductivity for Stamp-Transferrable Electrodes. *J. Am. Chem. Soc.* **2013**, *135*, 5144−5151.
(41) Tsai, Y. S.; Hung, C. H.; Chan, W. L.; Tsai, S. J.; Lee, Y. S.; Chang Huang, W.; Wu, Y. C. S.; Chen, H. Morphological and Crystalline Analysis of ZnO/ZnS Nanostructures on Porous Silicon Substrate. *Vacuum* **2020**, *178*, No. 109454.
(42) Kim, K.-H.; Kumar, B.; Lee, K. Y.; Park, H.-K.; Lee, J.-H.; Lee, H. H.; Jun, H.; Lee, D.; Kim, S.-W. Piezoelectric Two-Dimensional Nanosheets/Anionic Layer Heterojunction for Efficient Direct Current Power Generation. *Sci. Rep.* **2013**, *3*, No. 2017.
(43) Potu, S.; M, N.; Rajaboina, R. K.; Gollapelli, B.; Vallamkondu, J.; Mishra, S.; Divi, H.; Babu, A.; K, U. K.; Kodali, P. High-Performance and Low-Cost Overhead Projector Sheet-Based Triboelectric Nanogenerator for Self-Powered Cholesteric Liquid Crystal, Electroluminescence, and Portable Electronic Devices. *ACS Appl. Energy Mater.* **2022**, *5*, 13702−13713.
(44) Guguloth, L.; Singh, K.; Channu, V. S. R.; Kumari, K. Improved Performance of Ternary Blend Polymer Solar Cells via Work Function Tuning and Suppressed Interface Recombination Using Hybrid PEDOT:PSS-Graphene Oxide Hole Transport Layer. *Appl. Surf. Sci.* **2021**, *540*, No. 148266.
(45) Cao, Z.; Wu, Z.; Ding, R.; Wang, S.; Chu, Y.; Xu, J.; Teng, J.; Ye, X. A Compact Triboelectric Nanogenerator with Ultrahigh Output Energy Density of 177.8 J M−3 via Retarding Air Breakdown. *Nano Energy* **2022**, *93*, No. 106891.
(46) Zhu, G.; Chen, J.; Liu, Y.; Bai, P.; Zhou, Y. S.; Jing, Q.; Pan, C.; Wang, Z. L. Linear-Grating Triboelectric Generator Based on Sliding Electrification. *Nano Lett.* **2013**, *13*, 2282−2289.
(47) Tantraviwat, D.; Ngamyingyoud, M.; Sripumkhai, W.; Pattamang, P.; Rujijanagul, G.; Inceesungvorn, B. Tuning the Dielectric Constant and Surface Engineering of a BaTiO3/Porous PDMS Composite Film for Enhanced Triboelectric Nanogenerator Output Performance. *ACS Omega* **2021**, *6*, 29765−29773.
(48) Wang, Y.; Duan, J.; Yang, X.; Liu, L.; Zhao, L.; Tang, Q. The Unique Dielectricity of Inorganic Perovskites toward High-Performance Triboelectric Nanogenerators. *Nano Energy* **2020**, *69*, No. 104418.
(49) Paria, S.; Si, S. K.; Karan, S. K.; Das, A. K.; Maitra, A.; Bera, R.; Halder, L.; Bera, A.; De, A.; Khatua, B. B. A Strategy to Develop Highly Efficient TENGs through the Dielectric Constant, Internal Resistance Optimization, and Surface Modification. *J. Mater. Chem. A* **2019**, *7*, 3979−3991.
(50) Das, N. K.; Nanda, O. P.; Badhulika, S. Piezo/Triboelectric Nanogenerator from Lithium-Modified Zinc Titanium Oxide Nanofibers to Monitor Contact in Sports. *ACS Appl. Nano Mater.* **2023**, *6*, 1770−1782.
(51) Mainra, J. K.; Kaur, A.; Sapra, G.; Gaur, P. Simulation and Modelling of Triboelectric Nanogenerator for Self-Powered Electronic Devices. *IOP Conf. Ser.: Mater. Sci. Eng.* **2022**, *1225*, No. 012012.
(52) Zou, H.; Zhang, Y.; Guo, L.; Wang, P.; He, X.; Dai, G.; Zheng, H.; Chen, C.; Wang, A. C.; Xu, C.; Wang, Z. L. Quantifying the Triboelectric Series. *Nat. Commun.* **2019**, *10*, No. 1427.
(53) Varghese, H.; Chandran, A. A Facile Mechanical Energy Harvester Based on Spring Assisted Triboelectric Nanogenerators. *Sustainable Energy Fuels* **2021**, *5*, 5287−5294.
(54) Cui, N.; Gu, L.; Lei, Y.; Liu, J.; Qin, Y.; Ma, X.; Hao, Y.; Wang, Z. L. Dynamic Behavior of the Triboelectric Charges and Structural Optimization of the Friction Layer for a Triboelectric Nanogenerator. *ACS Nano* **2016**, *10*, 6131−6138.
(55) Lacks, D. J.; Sankaran, R. M. Contact Electrification of Insulating Materials. *J. Phys. D: Appl. Phys.* **2011**, *44*, No. 453001.
(56) Han, K.; Tang, W.; Chen, J.; Luo, J.; Xu, L.; Wang, Z. L. Effects of Environmental Atmosphere on the Performance of Contact−Separation Mode TENG. *Adv. Mater. Technol.* **2019**, *4*, No. 1800569.
(57) Dudem, B.; Huynh, N. D.; Kim, W.; Kim, D. H.; Hwang, H. J.; Choi, D.; Yu, J. S. Nanopillar-Array Architectured PDMS-Based Triboelectric Nanogenerator Integrated with a Windmill Model for Effective Wind Energy Harvesting. *Nano Energy* **2017**, *42*, 269−281.

https://doi.org/10.1021/acsami.3c04848
ACS Appl. Mater. Interfaces 2023, 15, 33095−33108

(58) Li, X.; Zhang, C.; Gao, Y.; Zhao, Z.; Hu, Y.; Yang, O.; Liu, L.; Zhou, L.; Wang, J.; Wang, Z. L. A Highly Efficient Constant-Voltage Triboelectric Nanogenerator†. *Energy Environ. Sci.* **2022**, *15*, 1334−1345.
(59) Liu, D.; Yin, X.; Guo, H.; Zhou, L.; Li, X.; Zhang, C.; Wang, J.; Wang, Z. L. A Constant Current Triboelectric Nanogenerator Arising from Electrostatic Breakdown. *Sci. Adv.* **2019**, *5*, No. eaav6437.
(60) Qin, H.; Gu, G.; Shang, W.; Luo, H.; Zhang, W.; Cui, P.; Zhang, B.; Guo, J.; Cheng, G.; Du, Z. A Universal and Passive Power Management Circuit with High Efficiency for Pulsed Triboelectric Nanogenerator. *Nano Energy* **2020**, *68*, No. 104372.

https://doi.org/10.1021/acsami.3c04848
ACS Appl. Mater. Interfaces 2023, 15, 33095−33108